LARGE APERTURE X-RAY MONITORS FOR BEAM PROFILE DIAGNOSTICS

Cyrille Thomas*, Guenther Rehm, Diamond, Oxfordshire, UK
Frederike Ewald, ESRF, Grenoble, France
John Flanagan, KEK, Tsukuba, Japan

Abstract

Emittance is one of the main characteristic properties of a beam of particles in an accelerator, and it is measured generally by means of the particle beam profile. In particular, when the beam of particles is emitting an X-ray photon beam, a non perturbative way of measuring the particle beam profile is to image it using the emitted X-ray photon beam. Over the years, numerous X-ray imaging methods have been developed, fulfilling the requirements imposed by a particle beam becoming smaller, and approaching micron size for electron beam machine with vertical emittance of the order of 1 pm-rad. In this paper, we will first recall the properties of the X-ray photon as function of source and its properties. From this we will derive some natural definition of a large aperture X-ray imaging system. We will then use this selection criterion to select a number of X-ray imaging devices used as a beam profile diagnostics in an attempt to give an overview of what has been achieved and what is possible to achieve with the selected devices.

INTRODUCTION

For a synchrotron radiation (SR) light source the emittance is the main parameter that describes its ultimate performance, as it is inversely proportional to the brilliance of the emitted SR. From the first SR light source to the latest ones under construction or proposed to be built in the next decade, the emittance has been reduced from thousands of nm.rad to nm.rad and even less. One of the main diagnostics for the emittance, and the emittance coupling (or vertical emittance) is a measurement of the beam transverse size, which is proportional to the square-root of the emittance. As a result of the emittance reduction, the transverse beam size as also been reduced to the range of 1 to 20 µm, and the vertical emittance to 0.1 to several µm. Therefore, the measurement of beam profile and beam size is becoming more and more challenging, due to the high resolution imposed on the profile measurement system. A natural way to measure the beam profile and thus the emittance, is to image the particle beam using the SR. Since the resolution required for the very small beam size is in the µm range, large aperture imaging system and small wavelengths becomes a logical choice for such a measurement. In particular, large aperture X-ray imaging systems seem particularly adapted, as they provide the required sub-micrometer resolution. In this paper, we will review the large aperture X-ray beam profile measurements systems that have been developed so far. Before that, we will refer to the work referenced in [1–4], on the properties of the SR sources and their image. This will then provide a definition of what is understood by *Large Aperture* for an X-ray imaging system imaging a SR source. Using the Fourier Optics, we will recall and illustrate relations between resolution of an imaging system and its Point Spread Function. In the same section, we will also report on deconvolution techniques, which are the natural following step to extract from the image most of the information about the source. We will see later that some of the imaging systems presented here cannot be operated without deconvolution, in particular the class of imaging systems that constitute the coded apertures. This class of systems include Uniformly Redundant Array (URA), Optimized RAndom pattern (ORA), Hexagonal URA (HURA), Modified URA (MURA), but also Fresnel Zone Plate (FZP). We will report on measurements of very small beam sizes using two of these systems. One is a URA and requires deconvolution to extract information from the image, and the other is a FZP. For the case of a FZP the diffraction limit point spread function has a width of the order of the outer rings difference, which is in the nm range for X-ray. As a consequence the resolution is generally good enough so that deconvolution is not required. We will report on beam profile measurement with FZP, but also on the new technologies for making diffraction limited FZP for hard X-ray. Another class of large aperture X-ray imaging systems is known as Compound Refractive Lenses (CRLs). In this section we will report on the state of the art in making CRLs and we will illustrate with beam profile measurements and their performances. Finally, before concluding, we will be discussing the commissioning, operation, cost and performance of these systems and compare them to a small aperture X-ray beam profile diagnostic which is the X-ray pinhole camera.

SR X-RAY SOURCES

The SR X-ray source, i.e. the relativistic charged particle beam in a bending magnet or in an undulator has been described by G. Geloni *et al.* in a series of papers [1–4]. As it is shown in these series, SR is a random stochastic process, and as such the laws of Statistical Optics must be applied to solve the image formation problem. In some cases, Statistical Optics is not the only possible description of the formed images. For instance, in the case of an undulator SR, it is shown that for a beam emittance much larger that the wavelength diffraction limit, Geometrical optics coincides with the Statistical Optics description of the SR. In the follow-

* cyrille.thomas@diamond.ac.uk

ISBN 978-3-95450-127-4

ing we will try to summarise some of the main results for X-ray SR.

Bending Magnet SR

As shown in [1], the bending magnet SR properties for imaging can be fully described by its transverse mutual coherence. For X-ray, the source appears to be quasi-homogeneous, and satisfies the condition for which Geometric Optics can be used for the image formation problem. This condition is expressed as follow:

$$C = max\left[\frac{2\pi\varepsilon\beta}{\lambda L_f},1\right]\cdot max\left[\frac{2\pi\varepsilon L_f}{\beta\lambda},1\right] \gg 1 \qquad (1)$$

where ε is the horizontal or vertical emittance, β is the betatron function at the source, λ is the wavelength at which the SR is observed, and L_f is the radiation formation length and is defined for a bending magnet by $L_f = (\frac{\lambda\rho}{2\pi})^{\frac{1}{3}}$, with ρ the bending radius. For 3rd generation light sources, where vertical emittance can be of the order of 1 pm.rad, a bending radius of the order of 10 m, for $\lambda \simeq 0.1$ nm, the radiation formation length is of the order of 0.5 mm and $C \simeq 2000$, so the necessary condition for which Geometric Optics can be used is satisfied. It follows that when investigating the image formation of the source, one can use either Fourier Optics together with Statistical Optics description of the source, or Geometrical Optics with ray tracing techniques, whichever of the method appears the most suitable to the problem to be solved. Any imaging system can be treated by means of Fourier Optics, in which operators are propagating the source through the optics elements of the experimental setup. With incoherent imaging, the propagation operator is linear in intensity. The electric field distribution and associated phase have been described in many papers [1, 5] and implemented in computer codes like for instance SRW [6] and SPECTRA [7]. The equation for the electric field for a single electron with offset $l_{x,y}$ and angle $\eta_{x,y}$ (equation (82) of reference [1]) is reported below:

$$\tilde{\mathbf{E}} = \frac{i\omega e}{c^2 z_o} e^{i\Phi_s} e^{i\Phi_o} \int_{\infty}^{\infty} dz \left(\frac{z}{\rho}\hat{\mathbf{x}} + (\theta_y - \eta_y)\hat{\mathbf{y}}\right) e^{i\omega\left[\frac{z}{2\gamma^2 c}\left(1+\gamma^2(\theta_y-\eta_y)^2\right)+\frac{z^3}{6\rho^2 c}\right]} \qquad (2)$$

with

$$\Phi_s = \frac{\omega z_o}{2c}\left(\theta_x^2 + \theta_y^2\right) \qquad (3)$$

and

$$\Phi_o = -\frac{\omega\rho\,(\theta_x - \eta_x)}{2c}\left(\frac{1}{\gamma^2} + (\theta_y - \eta_y)^2 + \frac{(\theta_x - \eta_x)^2}{3}\right) - \frac{\omega}{c}\left(l_x\theta_x + l_y\theta_y\right) \qquad (4)$$

and $\hat{\mathbf{x}}$, $\hat{\mathbf{y}}$ are the unit polarisation vectors in the horizontal and vertical planes; ρ is the bending radius; $\theta_{x,y}$ is the observer angle from the source; $\omega = \frac{2\pi}{\lambda}$ is the frequency (λ the wavelength) at which the SR is observed; c the speed of light.

This expression shows the phase of the electric field to be different from the spherical quadratic phase coming from a point source. As a result, the point spread function (PSF) is somehow blurred compared to the PSF of a point source. The intensity of the field given by the square modulus of the integral is constant in the horizontal plane and has a finite distribution in the vertical plane. The integral can be expressed by either Airy functions or Bessel functions. In the vertical plane, the function is even with the vertical angle variable, goes through a maximum and decreases towards zero with large angles. The vertical intensity profile has a width which defines an opening angle[1] for the beam θ_{BM}:

$$\theta_{BM} \simeq \frac{1}{\gamma}\left(\frac{\omega}{\omega_c}\right)^{-0.425} \qquad (5)$$

The finite distribution in the vertical plane is limiting the resolution of an imaging system to the natural opening vertical angle of the photon beam. In the horizontal plane, the resolution will be limited by the opening angle of the imaging system observing the source. This will be discussed in the next section.

Finally, another important parameter for the SR is the flux of photons impinging on an imaging aperture. This expression is given by:

$$\frac{d\Phi}{d\Omega}_{[Photons/0.1\%BW/mrad^2]} = 1.237 \times 10^{13} E^2_{[GeV]} I_{[A]}\, y^2\left(1+X^2\right)\left[K^2_{2/3}(\xi) + \frac{X^2}{1+X^2}K^2_{1/3}(\xi)\right] \qquad (6)$$

where $y = \frac{\omega}{\omega_c}$, and $\omega_c = \frac{3c\gamma^2}{2\rho}$ is the critical frequency, $X = \gamma\theta_y$, $\xi = \frac{\omega\rho}{3c}\left(\gamma^{-2} + \theta_y\right)^{\frac{3}{2}}$; $K^2_\nu(\xi)$ is the first order modified Bessel function of order ν.

From Eq. 6 it can be seen that the number of photons/s impinging on a large aperture is of the order of 10^{10} close to the critical photon beam energy.

Undulator SR

The undulator SR and coherence properties of this source has been extensively studied in [2, 4]. As function of the beam size and divergence in the undulator, and for a given wavelength, it can be shown that the non-stationary source may be non-homogeneous (coherent or partially coherent) with non-Gaussian distribution, and in some other cases the source is quasi-homogeneous and is described by the Gaussian distribution of the relativistic particles' beam.

[1] The opening angle for the bending magnet and the undulator given here are $\theta = 2\sigma$, with σ the r.m.s value of the Gaussian fitting the angular profile

ISBN 978-3-95450-127-4

In this case Geometrical Optics can apply to the image formation problem. The different cases depend on the values of $\hat{N} = \frac{\sigma_{x,y}^2 \omega}{c L_w}$ and $\hat{D} = \frac{\sigma_{x',y'}^2 \omega L_w}{c}$, the normalised square beam size, and the normalised square beam divergence, respectively; $\sigma_{x,y}$ and $\sigma_{x',y'}$ are the beam size and divergence, and L_w is the undulator length.

- Case $N_x \gg 1$ and $D_x \gg 1$: In this case, the source can be considered quasi-homogeneous in the horizontal plane. Moreover, the cross-spectral density can be factorised in two functions of horizontal and vertical variables. In addition, in the horizontal plane, the source can also be described by Geometrical Optics, and the virtual source corresponds to the beam distribution.
  1. Case $N_y \gg 1$ and $D_y \gg 1$: this is the same situation as for the case of Case $N_x \gg 1$ and $D_x \gg 1$, but in the vertical plane.
  2. Case $N_y \gg 1$ and $D_y > 0$: this corresponds also to a situation in which the image of the source through a lens will correspond to the beam distribution.
  3. Case $N_y > 0$ and $D_y \gg 1$: This is the case of a source with non-Gaussian distribution in the vertical direction. The image of the source in the vertical plane does not correspond to the beam vertical distribution, but is a convolution of the beam distribution with a universal function $\hat{\mathrm{B}}$ (see Eq. (186) in [4]. In the particular case of $N_y \ll 1$, which corresponds to the diffraction limit case, the image profile is described by the universal function $\hat{\mathrm{B}}$. The source is non-homogeneous.
  4. Case $N_y \ll 1$ and $D_y \ll 1$: This is the fully vertical diffraction limited case, the source is non-homogeneous, and the image of the source through a lens is described by a universal function Ψ given by Eq. (95) in [4]
- Case $N_x > 0$ and $D_x \ll 1$: In this case, we have automatically $N_y \ll 1$ and $D_y \ll 1$ so that the source is diffraction limited in the vertical plane. The image of the source is given by Eq. (387) of [4]. It is not Gaussian and is the convolution of a universal function given by Eq. (386) of [4] and the beam horizontal distribution. In the case of $N_x \ll 1$, corresponding to the case of a diffraction limited source in both horizontal and vertical planes, the image is given by the scaled universal function, Eq. (388) of [4].

In all these cases, the SR beam propagates from the undulator to the imaging system and has a defined aperture, which for the n$^{\mathrm{th}}$ harmonic has an opening angle of the order of

$$\theta_{u,n} = \sqrt{\frac{n\left(1+K^2/2\right)}{2N_w\gamma^2}} \tag{7}$$

N_w is the number of undulator periods, and K is the undulator deflection parameter. As for the vertical opening angle of the bending magnet, this finite opening angle defines a limited resolution for the imaging of the source.

Finally, the flux of photons in the n$^{\mathrm{th}}$ odd harmonic of a planar undulator is given by the following equation:

$$\frac{d\Phi_n}{d\Omega}_{[Photons/s/0.1\%BW/mrad^2]} = 1.744 \times 10^{14} N_w^2 E_{[GeV]}^2 I_{[A]} F_n(K) \tag{8}$$

and

$$F_n(K) = \frac{n^2K^2}{1+\left(K^2/2\right)^2} \left(J_{(n-1)/2}\left(\frac{nK^2}{4+2K^2}\right) - J_{(n+1)/2}\left(\frac{nK^2}{4+2K^2}\right)\right)^2 \tag{9}$$

with $J_m(X)$ the modified Bessel function of the first kind of order m and variable X.

It follows that for a first harmonic of a planar undulator with 100 periods, $K = 2$, electron energy $E = 3$ GeV, and a current $I = 300$ mA, the flux of photons is of the order of first odd harmonics is of the order of 10^{18} photons/s/0.1% bandwidth.

POINT SPREAD FUNCTION, RESOLUTION, DECONVOLUTION TECHNIQUE

The description of the SR source showed that SR propagates as a beam with a narrow opening angle. This directionality of the beam implies the beam is partially coherent in front of an imaging system. As a consequence, the general treatment to solve the image problem imposes knowledge of the spectral degree of coherence of the beam in front of the imaging system. In addition, the opening angle of the SR can be seen by means of the Fourier Optics as a natural limiting aperture applied in front of an imaging system. In that sense, we will first define as a large aperture X-ray imaging system any X-ray imaging device that has a non-limiting aperture to the SR beam. Following this, the PSF of the system, defined as the spatial Fourier Transform of the product of the autocorrelation of the aperture of the imaging system and the spectral degree of coherence, is dominated by the natural aperture of the SR beam.

In the previous section we have seen that for the bending magnet SR, the horizontal opening angle is defined by the aperture system intercepting the arc of emitted SR, and the vertical opening angle is given by Eq. 5. Besides, for X-ray and very small emittance beam, the condition given by Eq. 1 is always satisfied so that Geometrical Optics can be used to find out the image of the beam. As a consequence, the PSF is expected to be a peaked function decreasing non necessarily monotonically to zero at infinity. The width of the PSF is also expected to be inversely proportional to the

ISBN 978-3-95450-127-4

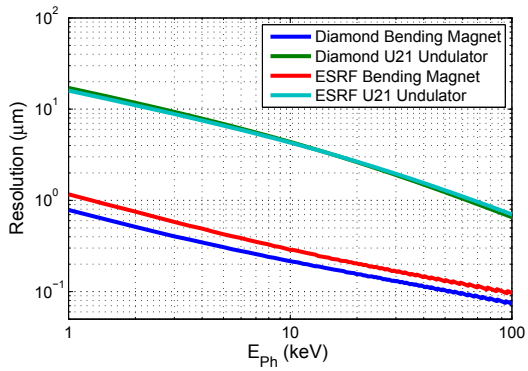

Figure 1: Resolution for an ideal aberration free large aperture X-ray imaging system.

aperture of the imaging system in the horizontal plane, and to the beam aperture in the vertical plane. The resolution Δ_{BM} of the imaging system can be defined as the width of the PSF, and is expected to be of the order of:

$$\Delta_{BM} \simeq \frac{\lambda}{2\sin(\theta_{BM})} \simeq \frac{\lambda}{2\theta_{BM}} \tag{10}$$

as θ_{BM} is always a very small angle.

Similarly, for the case of the undulator SR, and for the cases when the Geometrical Optics apply, the PSF width will be defined as:

$$\Delta_{U} \simeq \frac{\lambda}{2\sin(\theta_{U})} \simeq \frac{\lambda}{2\theta_{U}} \tag{11}$$

In the case of very small emittance in the diffraction limited cases, it appears that Geometrical Optics cannot be used to solve the image formation problem, and that the image is not a scaled profile of the source. The use of undulator SR for beam profile diagnostics has to be questioned and wavelength carefully chosen in order to avoid a diffraction limited source.

Figure 1 shows numerical examples for the vertical resolution, taking the case of Diamond and ESRF, for the case of the bending magnet SR and a similar undulator with 90 periods, 2 m long. Clearly, the case of the bending magnet SR is most favorable.

Deconvolution Techniques

It is clear from Fourier Optics [8] that for a given imaging system, the object to be imaged is convolved with the impulse response of the imaging system, i.e. the PSF. Without any processing, the resolution is given by the width of the PSF. However, it has been long seen and investigated that the information on the image can be restituted by means of deconvolution, and provided a very good knowledge of the PSF of the system. Since imaging systems are mostly sensitive to the intensity of the signal, incoherent imaging favours deconvolution techniques because the system is linear in intensity [8]. Partially coherent systems will present speckled images that are difficult to deconvolve due to the non-linearity in intensity of the system. For incoherent imaging, many algorithm for image deconvoltion exist and this is a very active research area in applied mathematics and applied optics. We will simply present here some of the concepts and illustrate image deconvolution with a set of pinhole apertures as shown in [9].

An image can be mathematically described by the convolution of the object intensity profile with the intensity impulse response of the imaging device as:

$$i(x,y) = h(x,y) \otimes o(x,y) + n(x,y) \tag{12}$$

where $i(x,y)$ is the image describe in 2-D coordinates, $h(x,y)$ is the impulse response of the system and $n(x,y)$ is the noise in the system. In any acquisition system, the presence of noise is inevitable, and requires to be introduced in the model. Fourier Transform (FT) of Eq. 12 is shown below, using the FT convolution properties.

$$I(\nu,\eta) = H(\nu,\eta) \cdot O(\nu,\eta) + N(\nu,\eta) \tag{13}$$

It appears that without any noise, and with the knowledge of $h(x,y)$ and thus $H(\nu,\eta)$, the object can be totally recovered. The introduction of the noise transforms the problem into an ill-posed problem, which is addressed by many deconvolution algorithms. An example of image deconvolution algorithm is the Lucy-Richardson (LR) algorithm[10, 11]. It is an iterative converging algorithm as shown in [12, 13] which assumes noise to be dominated by Poisson statistics, which is characteristic to the photon noise. An example of image deconvolution using LR algorithm is shown in [9], where a series of pinholes from 5 μm to 100 μm has been used to image a 3 GeV electron beam in a bending magnet with a vertical size $\sigma_v = 5\,\mu$m. The results of the deconvolution shows that even for a 100 μm pinhole aperture, the retrieved vertical image size is converging to 5 μm. However, we want to put an emphasis on the knowledge of the PSF. The restitution of the object will be very precise but only to the accuracy of the PSF description. The PSF might be measured, or modeled and generated numerically as in [9].

Performance of a deconvolution is dependant on the model of the PSF, but also on the model of the noise. In the following we will see that for the coded apertures, deconvolution is necessary to recover the image, and indeed, the noise in the image plays a role in the uncertainty of the measured beam size.

CODED APERTURES

The concept of coded aperture has be first introduced by Dicke [14] and Ables [15]. In this original version, the aperture was simply a collection of pinholes randomly distributed. They were used for X-ray and gamma-rays imaging when no lenses were invented, and in order to increase the flux through a single pinhole camera. Later, new arrangement were developed with the apparition of URA [16], and later MURA [17]. Coded apertures are a large

ISBN 978-3-95450-127-4

class of lensless imaging devices which consist in an array of opaque and transparent elements, which placed between an illuminated object or a source and an intensity recording device, produce a shadowgram that can be processed to recover the object from the coded image. URAs have been applied only recently as an X-ray beam profile diagnostics [18–21]. We will see they could provide information about beam size and position bunch by bunch and turn by turn. FZPs also have been used for the measurement of beam profile and emittance [22] reporting on a 4 µm vertical beam size [23].

URAs, MURAs, HURAs

The particularity of the URAs, MURAs, HURAs coded apertures is that they are built with the use of a class of function called pseudo-noise functions. For instance an URA is built as follow:

The aperture A is divided in a $r \times s$ array with r,s prime numbers and $r - s = 2$, and each element of the array is either transparent $A(i,j) = 1$ or opaque $A(i,j) = 0$ following the rules:

$$A(i,j) = \begin{cases} 0, & \text{if } i = 0 \\ 1, & \text{if } j = 0, i \neq 0 \\ 1, & \text{if } Q_r(i)Q_r(j) = 1 \\ 0, & \text{if } Q_r(i)Q_r(j) = -1 \end{cases} \quad (14)$$

where the quadratic residue Q_r is:

$$Q_r(p) = \begin{cases} 1, & \text{if} \exists x \subset \mathbb{N} \text{and} 1 \leq x < r \\ & \text{such that } p = mod_r\left(x^2\right) \\ -1, & \text{otherwise} \end{cases}$$

With this pattern, the flux transmitted to the detector in the image plane is 50% of flux that would pass through the whole aperture area. This can be several orders of magnitude compared to the flux transmitted by a pinhole with the unit cell area $A(i,j)$.

The pattern of the coded aperture is chosen so that the convolution with the decoding mask is a Dirac function. For an URA, the decoding function, G can be built as

$$G(i,j) = \begin{cases} 1, & \text{if } A(i,j) = 1 \\ -1, & \text{if } A(i,j) = 0 \end{cases} \quad (15)$$

This way, retrieving the object from the coded image can be expressed as:

$$\hat{O} = I \otimes G = ((O+N) \otimes A) \otimes G \quad (16)$$

Here we have introduce the noise (N) on the image. As suggested by Eq. 16, noise but also diffraction and scattering [19, 21] may prevent the recovering of the object with the direct deconvolution, and more advanced deconvolution or convolution algorithms may be used.

The resolution of an URA can be estimated with the evaluation of its Modulation Transfer Function (MTF), which is the FT of the system PSF. MTF for an URA has been derived in Eq. (17) of [24]:

$$MTF_{[URA]} = \mathscr{F}(A \otimes G_\delta \otimes D \otimes Q) \quad (17)$$

where $\mathscr{F}$ if the FT, $A \otimes G_\delta$ the system PSF, D the single element PSF, and Q the detector PSF. It shows that in the ideal case, the MTF of the URA is equal to the single pinhole MTF.

We have briefly described here URA as an example of coded aperture. However, many more coded aperture exist and have been designed to further improve the robustness of the object reconstruction. For instance, MURA, and HURA can be decoded using a unimodular valued correlation inverse G for which the signal to noise becomes uniform and insensitive to the source structure [17].

Fresnel Zone Plates

From the first FZPs [25] used to produce X-ray images to nowadays, the techniques for making them have been constantly evolving to produce highly efficient FZPs for hard X-ray [26]. The main challenges in making FZPs for hard X-ray comes from the combined necessity to have alternating opaque transparent rings separated by a radius difference of the order of tens of nm to ensure a very small diffraction limited spot size together with the large thickness of the opaque material to ensure a high efficiency of the diffraction orders. The diffraction limited spot, i.e. PSF of the FZP is of the order of the outer rings radii difference of the FZP. The n$^{\text{th}}$ radius of a FZP is given by:

$$r_n = \sqrt{n\lambda f + \frac{n^2\lambda^2}{4}} \quad (18)$$

where λ is the wavelength at which the FZP is designed, f is the focal length (of the first diffraction order). Eq. 18 shows FZPs to be highly sensitive to chromatic aberrations. Using Eq. 18, for 8 keV photon energy ($\lambda = 0.15$ nm), $f =$ 0.25 m, and n = 11000, the difference of the outer rings is of the order of 20 nm.

The diffraction efficiency, taking into account the phase shift of the absorbing material is given by [27] and for a perfect FZP

$$E = \left(\frac{1}{\pi q}\right)^2 \left(1 + e^{-4\pi\frac{T\beta}{\lambda}} - 2e^{-2\pi\frac{T\beta}{\lambda}} \cos 2\pi \frac{T\delta}{\lambda}\right) \quad (19)$$

with β and δ the material index coefficient for absorption and phase shift across the length of material T. An example for gold is given in Fig. 2. It shows that at 2 keV, the efficiency of the first order diffraction is 23% for a thickness of 500 nm. For the same thickness, it drops to 7% at 8 keV. The height to width aspect ratio structure is in this case larger than 30. It illustrates the manufacturing difficulties encountered in the production of high resolution hard X-ray FZP.

Nevertheless, FZPs have been used to measure the beam profile at ATF-KEK [22]. The system is a combination of

ISBN 978-3-95450-127-4

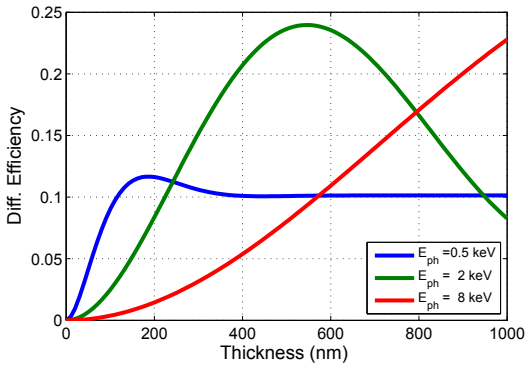

Figure 2: Diffraction efficiency of a FZP, as given by Eq. 19.

2 FZPs in a telescope assembly which provide a magnification $\times 20$, and a resolution of the order of 0.7 µm. The smallest vertical beam size measured is of the order of 4µm after suppression of 100 Hz vibration that was causing a motion blur on the image. One of the remarks to be made is that the image of the beam (Fig. 10 from [22]) are quite specular. This is because the number of photons for the image is small enough to be able to count them. Indeed, a rough estimate shows that 10^6 photons/ms illuminate the FZP assembly, and taking into account 20% efficiency for each FZPs of the assembly, the number of photons illuminating the camera is approximatively of the order of 10^4 photons. In their case the illuminated CCD area at FWHM is $\approx 50 \times 12$ pixels, which imposes the use of a highly linear camera, sensitive to single photons.

COMPOUND REFRACTION LENSES

The first CRLs invented and used [28], where applied to focus SR X-ray beam. Similarly to FZPs, CRLs are mainly used for SR X-ray micro and nano-focus experiments rather that beam diagnostics. However, like FZPs, CRLs can be used to image the SR source offering a similar resolution, and a larger transmission. As shown in [29], abberation of a CRL depends on the shape of the lens surface. For parabolic shape, aberration is pronounced and by far the largest as compared to elliptical shapes or Cartesian oval shape which appears to be the natural surface shape solution for a point source. As shown in Fig. 7 of [29], for large aperture, aberration appears to be significantly larger than the Airy disk width, which is the PSF of a perfect circular aperture. This shows that the shape of the surface of the lens has to be chosen as function of the source. For a bending magnet source, the specific shape could be found with the use of Statistical Optics as seen in the above section. Beam profile has been measured using CRLs [30], on a bending magnet SR source, at very high photon energy. Their expected resolution is supposed to match the beam resolution with an aperture of 0.450 mm at 4.5 m. However, at the high photon energies at which the beam is imaged, scattering may be an issue. Indeed, on the beam images, a background rises up making additional wings to the beam profile [30, 31]. Investigation for the source of this background is still ongoing, and no conclusion whether aberration of the parabolic lens or real scattering is the main contribution.

DISCUSSION AND CONCLUDING REMARKS

We have seen that SR sources are becoming more and more diffraction limited for hard X-ray SR beams, as a result of small emittances and thus small beam sizes, in the sub-µm range for the vertical. For the imaging of the source using large aperture systems, i.e. larger than the natural opening of SR, is it desirable to have quasi-homogeneous sources for which Geometrical Optics applies and coincides with the general description from the Statistical Optics. Large aperture systems offer a suitable resolution and can match the natural resolution offered by the SR beam itself. The resolution is certainly a parameter of the problem to look at in detail, but this is not the only one. We have seen that most of the larger aperture systems offer enough resolution to allow µm beam size to be measured. However, commissioning, cost and operation are other very important parameters to consider before selecting one or the other of these possible diagnostics. For the commissioning, all direct imaging systems, (FZPs, CRLs, etc.) should be rather straightforward because the perception of the image matches our representation. In the case of the indirect imaging systems, like the coded aperture where image processing is required, a large confidence has to be built in the image processing in order to answer the first question that comes after image is acquired: what is the emittance and the coupling? The cost comes next as some of the systems will need to include a monochromator and others not. This is an additional cost to the system and an additional system to commission too. Also this is an additional system that needs to be designed taking into account the large coherence area of diffraction limited SR. This will non-doubtably increase the surface tolerance of the monochromator and thus its cost. Also the addition of a monochromator constitutes another complete system with more diagnostics to match the design performance of the imaging systems that are highly chromatic, and ensure robustness in operation. Finally, the efficiency of the system is to be considered too. For the coded apertures, the flux transmitted is 50% of the total flux of the 'white' beam. This makes coded aperture a very sensitive system. As seen this is a system capable of measuring beam size of all individual bunches along a train. To match the performance, efforts and cost would have to be put on speed of the data acquisition, but also on computing power for the image processing.

In summary, none of the systems is ideal, FZPs or CRLs offer the best resolution and direct imaging, but with a poor sensitivity and additional system cost. Coded apertures offer enough resolution to measure ultra small beam sizes,

ISBN 978-3-95450-127-4

but require complex deconvolution using large computing power which is added also to the cost of the system.

We have focussed on large aperture X-ray imaging systems, but of course there are not the only possible imaging systems to be used for measuring micron size beams. For instance, a very simple, robust and cost effective imaging system is the X-ray pinhole camera. The PSF width might be larger than for these large aperture systems, but after deconvolution, beam sizes of the order of 5 µm have been measured at Diamond, corresponding to 1 pm.rad vertical emittance. Also the use of interferometry imaging technique, in the UV-visible, is capable to measure micron beam sizes whenever Van Cittert Zernike can apply, i.e. when the source is (quasi)-homogeneous. These system are also worth exploring as they can be quite robust, relatively straightforward measurements and also cost effective.

REFERENCES

[1] G. Geloni, *et al.*, *ArXiv Physics e-prints/0502120*, Feb. 2005.

[2] G. Geloni, *et al.*, *ArXiv Physics e-prints/0506231*, Jun. 2005.

[3] G. Geloni, *et al.*, *ArXiv Physics e-prints/0608145*, Aug. 2006.

[4] G. Geloni, *et al.*, *ArXiv Physics e-prints/0603269*, Mar. 2006.

[5] O. Chubar, *et al.*, *Nucl. Inst. and Meth. in Phys. Res. A*, 435(3):495-508, 1999.

[6] O. Chubar, *et al.*, *Proc. of EPAC 1998*, pages 1177–1179, Jun. 1998.

[7] T. Tanaka, *et al.*, *J. of Synchrotron Radiation*, 8(6):1221–1228, Nov. 2001.

[8] J.W. Goodman, *Introduction to Fourier Optics*, Roberts and Company Publishers, third edition, 2004.

[9] C. A. Thomas, *et al.*, *Proc. of BIW 2012*, page 116–119, Apr. 2012.

[10] W. H. Richardson, *J. Opt. Soc. Am.*, 62(1):55–59, Jan. 1972.

[11] L. B. Lucy, *Astronomical J.*, 79:745, Jun. 1974.

[12] L. A. Shepp, *et al.*, *Medical Imaging, IEEE Transactions on*, 1(2):113–122, Oct. 1982.

[13] G. Zech, *Nucl. Inst. and Meth. in Phys. Res. A*, 716:1–9, 2013.

[14] R. H. Dicke, *Astrophysics J.*, 153:L101, Aug. 1968.

[15] J. G. Ables, *Proc. of the Astr. Soc. of Australia*, 1:114, Feb. 1968.

[16] E E Fenimore, *et al.*, *Applied optics*, 17(3):337–47, Feb. 1978.

[17] S R Gottesman, *et al.*, *Applied optics*, 28(20):4344–52, Oct. 1989.

[18] J W Flanagan, *et al.*, *Proc. of EPAC 2008*, pages 1029–1031, Jun 2008.

[19] J W Flanagan, *et al.*, *Proc. of PAC 2009*, pages 3561–3563, May 2009.

[20] J W Flanagan, *et al.*, *Proc. of IPAC 2010*, pages 966–968, May 2010.

[21] J.W. Flanagan, *et al.*, *Proc. of DIPAC 2011*, pages 561–563, May 2011.

[22] H. Sakai, *et al.*, *Phys. Rev. S.T. A.B.*, 10(4):042801–18, Apr. 2007.

[23] T. Naito, *et al.*, *Proc. of IBIC 2012*, pages 215–217, Oct. 2012.

[24] E E Fenimore, *Applied optics*, 19(14):2465–71, Jul. 1980.

[25] L. Mertz, *et al.*, *Optical Instruments and Techinques*, page 305, 1962.

[26] S. Gorelick, *et al.*, *J. of Synchrotron Radiation*, 18(3):442–6, May 2011.

[27] S.-R. Wu, *et al.*, *Materials*, 5:1752–1773, Sep. 2012.

[28] A. Snigirev, *et al.*, *Nature*, 384:49–51, Nov. 1996.

[29] M. Sanchez del Rio, *et al.*, *J. of Synchrotron Radiation*, 19(Pt 3):366–74, May 2012.

[30] F. Ewald, *et al.*, *Proc. of DIPAC 2011*, pages 188–190, May 2011.

[31] F. Ewald, J.-C. Biasci, *Proc. of IBIC 2013*, WEPF12, Sept. 2013.

ISBN 978-3-95450-127-4